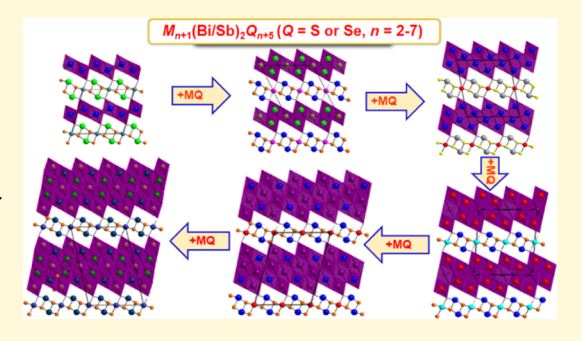
Downloaded by NORTHWESTERN UNIV at 12:09:13:531 on June 04, 2019 from https://pubs.acs.org/doi/10.1021/acs.chemmater.9b00585.

Six Quaternary Chalcogenides of the Pavonite Homologous Series with Ultralow Lattice Thermal Conductivity

Jing Zhao, * Shiqiang Hao, * Saiful M. Islam, *, Haijie Chen, Gangjian Tan, Shulan Ma, Shulan Ma, Shulan Ma, Shulan Ma, Gangjian Tan, Shulan Ma, Shulan M Christopher Wolverton, [§] and Mercouri G. Kanatzidis*, [‡]

Supporting Information

ABSTRACT: Six new quaternary chalcogenides belonging to the pavonite sulfosalt mineral family with the general formula $M_{n+1}(Bi/$ Sb)₂Q_{n+5} (n = 2-7) were synthesized by direct reactions of the elements at high temperatures. The compounds include $InPbBi_3S_7$ (n = 2), $In_{0.5}Mn_2Bi_{3.5}Se_8$ (n = 3), $CdPb_2Bi_4S_9$ (n = 4), $Ag_{1.5}CdBi_{5.5}Se_{10}$ (n = 5), $Ag_2CdBi_6Se_{11}$ (n = 6), and $Ag_{2.5}CdSb_{6.5}Se_{12}$ (n = 7) and crystallized in the monoclinic space group C2/m. The pavonite structure consists of two alternating slabs, a thinner slab composed of pairs of monocapped trigonal prisms separated by octahedra and a thicker slab with a galenalike structure motif. In the general formula, *n* corresponds to the number of octahedra along the diagonal direction of the galena-like slab. The



complex compositions, mixed occupancies of the cations, and quasi-two-dimensional structures endow compounds of this family with extremely low thermal conductivity. The charge and thermal transport properties of CdPb2Bi4S9 and CdAg2Bi6Se11 were characterized from 300 to 810 K, and both materials exhibited n-type semiconductor behaviors and ultralow lattice thermal conductivities of less than 0.35 W·m⁻¹·K⁻¹ for CdAg₂Bi₆Se₁₁ and 0.73 W·m⁻¹·K⁻¹ for CdPb₂Bi₄S₉ in the measured temperature range. Density functional theory calculations revealed the origins of this low lattice thermal conductivity to be a combination of the low Debye temperature, small phonon velocities, and large Grüneisen parameters. Thermoelectric properties were measured, and the highest ZT values of 0.53 and 0.95 for undoped CdPb2Bi4S9 and CdAg2Bi6Se11, respectively, were attained at 775 K.

■ INTRODUCTION

Phase homologies are regarded as "compound-generating machines" and provide a productive approach for designing inorganic structures with different modules. The structures of a homology are related to each other by a construction principle whereby the consisting modules resemble each other with an incremental difference by adding a layer or line of atoms.

The expansion of the number of synthetic inorganic materials provides a large database that can be used by scientists to investigate the relationship between structures, look for novel phenomena and quantum behavior, test theoretical predictions, and identify technologically enabling materials. Several chalcogenide homologies have been reported, enabling the forecasting of precise inorganic structures which can also be used as raw materials to improve thermoelectric (TE) performance through proper design.²⁻⁶ Examples include chalcogenides such as $(Sb_2Te_3)_m(Sb_2)_n^7$ $[MTe]_n[Bi_2Te_3]_m (M = Ge, Sn, Pb),$

$$\begin{split} & \big[(PbSe)_5 \big]_n \big[(Bi_2Se_3)_3 \big]_m,^{10-12} & Cs_4 \big[Bi_{2n+4}Te_{3n+6} \big],^{13} \\ & CsM_mBi_3Te_{5+m},^{14} & A_m \big[M_{1+l}'Se_{2+l} \big]_{2m} \big[M_{2l+n}''Se_{2+3l+n} \big] & (A = alkali) \end{split}$$
and alkali-earth element; M' and M'' = main group element),¹³and $[BiQX]_2[Ag_xBi_{1-x}Q_{2-2x}X_{2x-1}]_{n+1}$ (Q = S, Se; X = Cl, Br; $1/2 \le x \le 1$). Many of these families harbor exotic materials such as topological insulators and superconductors. Homologous structure design is especially important for incrementally tuning material properties, including optical properties, thermal conductivities, and electrical conductivities. 16 Mineral structures are generally stable with good tolerance to cations of different radii and can serve as a prototype for designing new compounds by elaborately selecting elements or tailoring the structure. The potential of some mineral homologous series, including the cannizzarite, ¹⁷ lillianite, ^{18,19} galenobismuthite, ¹⁷

Received: February 8, 2019 Revised: April 6, 2019 Published: April 9, 2019



[†]The Beijing Municipal Key Laboratory of New Energy Materials and Technologies, School of Materials Sciences and Engineering, University of Science and Technology Beijing, Beijing 100083, China

[‡]Department of Chemistry and [§]Department of Materials Science and Engineering, Northwestern University, Evanston, Illinois 60208, United States

Department of Chemistry, Physics and Atmospheric Sciences, Jackson State University, Jackson, Mississippi 39217, United States ¹State Key Laboratory of Advanced Technology for Materials Synthesis and Processing, Wuhan University of Technology, Wuhan 430070, China

and pavonite homologous series, 20,21 has already been demonstrated for TE applications. The pavonite structure type was defined by Makovicky et al. as an extensive series of complex sulfides in the Cu–Ag–(Pb)–Bi–S system 22,23 with the general chemical formula M_{n+1} Bi₂Q_{n+5}, where M is a five-or six-coordinated metal and the number n, as recorded in the literature, varies from 0 to 8; however, higher values of n are still possible. This homologous series is an important repository for targeting new types of semiconductors, including TE materials. New pavonite minerals are still being discovered in nature, $^{27-30}$ and the general properties of pavonite-type compounds have not been extensively investigated except for studies on the Cu_{x+y}Bi_{5-y}Q₈ (Q = S, Se) family. Secondary of the compounds have not been extensively investigated except for studies on the Cu_{x+y}Bi_{5-y}Q₈ (Q = S, Se) family.

In this work, we report the synthesis and crystal structures of six new quaternary chalcogenides belonging to the pavonite homologous series with n varying from 2 to 7, including InPbBi₃S₇ (n=2), In_{0.5}Mn₂Bi_{3.5}Se₈ (n=3), CdPb₂Bi₄S₉ (n=4), Ag_{1.5}CdBi_{5.5}Se₁₀ (n=5), Ag₂CdBi₆Se₁₁ (n=6), and Ag_{2.5}Cd₁Sb_{6.5}Se₁₂ (n=7). Phase-pure CdPb₂Bi₄S₉ and CdAg₂Bi₆Se₁₁ samples were prepared using high-temperature solid-state synthesis, and both of these compounds exhibited n-type semiconducting behavior and ultralow lattice thermal conductivities (<0.4 W/mK). Theoretical electronic structure calculations on CdPb₂Bi₄S₉ and CdAg₂Bi₆Se₁₁ suggest indirect band gaps and large Grüneisen parameters. Relatively high ZT values were attained for undoped CdPb₂Bi₄S₉ and CdAg₂Bi₆Se₁₁, suggesting their potential as TE materials.

EXPERIMENTAL SECTION

Reagents. Silver, bismuth, cadmium, indium, manganese, lead, and antimony with purities of 99.9% were purchased from Strem Chemicals, Inc.; sulfur pellets with a purity of 99.99% were purchased from Sigma-Aldrich, St. Louis, MO; and selenium pellets with a purity of 99.99% were purchased from American Elements, Inc. All the elements were used without any further purification.

Synthesis. All the reactants were weighed and loaded into a 9 mm fused-silica tube and flame-sealed under a vacuum pressure of $\sim 10^{-4}$ mbar.

InPbBi₃S₇ (n=2). The reaction of In (114.8 mg, 1 mmol), Pb (207.2 mg, 1 mmol), Bi (626.94 mg, 3 mmol), and S (224.7 mg, 7 mmol) in an evacuated silica tube resulted in InPbBi₃S₇ crystals. The samples was heated from room temperature (RT) to 1237 K over 18 h, held at this temperature for 12 h, cooled to 623 K over 32 h, held at this temperature for 18 h, and finally cooled to RT over 10 h. The obtained phase was impure, and Bi₄PbS₇ appeared as the second phase; the yield of InPbBi₃S₇ was estimated to be ~62% using JADE software (Materials Data, Inc., Livermore, CA, USA), and all the yield mentioned below were obtained using this software.

 $In_{0.5}Mn_2Bi_{3.5}Se_8$ (n=3). By high temperature reaction of In (114.8 mg, 1 mmol), Mn (54.9 mg, 1 mmol), Bi (626.94 mg, 3 mmol), and Se (552.72 mg, 7 mmol), $In_{0.5}Mn_2Bi_{3.5}Se_8$ crystals were obtained. The heating profile was the same as that of InPbBi₃S₇ mentioned above. The obtained sample contained a Bi₂Se₃ phase as an impurity; the yield of $In_{0.5}Mn_2Bi_{3.5}Se_8$ was approximately 93%.

 $CdPb_2Bi_4S_9$ (n=4). Crystals were obtained with starting elements of Cd (37.5 mg, 0.33 mmol), Pb (69.1 mg, 0.33 mmol), Bi (278.6 mg, 1.33 mmol), and S (85.5 mg, 2.67 mmol). The tube was heated from RT to 1123 K over 24 h, held at this temperature for 2 h, slowly cooled to 673 K over 72 h, held at this temperature for 1 h, and finally cooled to RT over 2 h. The yield of the target compound was approximately 30%, and the residual peak did not match that of any of the reported phases.

 $Ag_{1.5}CdBi_{5.5}Se_{10}$ (n = 5) and $CdAg_2Bi_6Se_{11}$ (n = 6). The two samples were obtained in the same reaction batch with starting elements of Cd (37.5 mg, 0.33 mmol), Ag (36.0 mg, 0.33 mmol), Bi

(299.5 mg, 1.43 mmol), and Se (210.6 mg, 2.67 mmol). The raw materials were heated from RT to 1053 K over 24 h, held for 32 h, slowly cooled to RT over 99 h. The synthesized samples contained both n = 5 and n = 6 phases, the proportions of which were 41 and 59%, respectively.

Ag_{2.5}Cd₁Sb_{6.5}Se₁₂ (*n* = 7). By reacting a mixture of Cd (56.2 mg, 0.5 mmol), Ag (107.9 mg, 1 mmol), Sb (365.4 mg, 3 mmol), and Se (434.5 mg, 5.5 mmol) crystals suitable for single-crystal X-ray diffraction (SCXRD) were obtained. The tube was heated to 1273 K over 18 h, held for 18 h, cooled to 823 K over 18 h, held at this temperature for 24 h, and finally cooled to RT over 10 h. The obtained sample was pure without any observable second phase.

For all these compounds, bulk crystals with lengths up to ${\sim}1$ mm were obtained.

Pure Phase Synthesis. $CdPb_2Bi_4S_9$ was obtained by high-temperature solid-state reaction with Cd (1125 mg, 10 mmol), Pb (4145 mg, 20 mmol), Bi (8360 mg, 40 mmol), and S (2885 mg, 90 mmol). The mixture was placed into a fused-silica tube with an outer diameter (OD) of 13 mm and flame-sealed under vacuum. The tube was heated from RT to 1237 K over 24 h, held at this temperature for 32 h, and quenched with water to RT. The obtained ingot was annealed at 823 K for 4 days.

 $CdAg_2Bi_6Se_{11}$ was synthesized by high temperature reaction of Cd (674.47 mg, 6 mmol), Ag (1391.50 mg, 12.9 mmol), Bi (7335.21 mg, 35.1 mmol), and Se (5211.36 mg, 66 mmol). The mixture was put into a tube with an OD of 13 mm and flame-sealed under vacuum. The sample was heated to 1237 K over 10 h, held at this temperature for 12 h, and water-quenched to RT. Powder X-ray diffraction (PXRD) measurements (details see in the Supporting Information) indicated that pure phases of $CdPb_2Bi_4S_9$ and $CdAg_2Bi_6Se_{11}$ were obtained.

Single-Crystal X-ray Diffraction (SCXRD). STOE IPDS II single-crystal diffractometer operating at 50 kV and 40 mA was used to conduct XRD measurements with Mo Kα radiation (λ = 0.71073 Å). The data collection was performed using X-Area software. X-RED was used to perform the integration, and X-SHAPE was used for numerical absorption corrections. X-RED and X-SHAPE are programs provided by STOE. The crystal structures were solved using direct methods and refined using the SHELXTL program package. Detailed information on the atomic occupancies, coordination numbers, and bond lengths of the title compounds is provided in Tables S1–S7.

Thermal Analysis. $CdPb_2Bi_4S_9$ and $CdAg_2Bi_6Se_{11}$ powder samples (approximately 70 mg) were placed into sealed fused-silica ampoules. Differential thermal analysis (DTA) was carried out by a Shimadzu DTA-50 thermal analyzer, and the sample was heated to 1273 K with a heating and cooling rate of ± 10 K/min. Afterward, the DTA products were collected and examined using PXRD.

Ultraviolet–Visible Spectroscopy. Diffuse-reflectance spectra collection was carried out using a Shimadzu UV-3600 spectrophotometer (double-beam, double-monochromatic) with BaSO₄ reference. The reflectance data were converted to absorbance data using the Kubelka–Munk equation.³⁴ The band gaps of the materials were estimated using a linear fit of the absorption edge.

Electrical Properties and Seebeck Coefficients. The pellets were cut into bars perpendicular to the direction of the sintering pressure. The conductivity and Seebeck coefficients were simultaneously obtained under a low pressure helium atmosphere using an UlvacRiko ZEM-3 instrument. The measurement uncertainty was approximately 5%. 35

Thermal Conductivity. The thermal diffusivity coefficients (D) were measured with the samples cut from the same spark plasma sintering (SPS)-processed pellet using a Netzsch LFA457 instrument. The thermal diffusivities were measured in the direction perpendicular to the sintering pressure direction. Analysis of the thermal diffusivity data was conducted using the Cowan model with pulse correction. The total thermal conductivity was calculated using the equation $\kappa_{\text{tot}} = DC_p d$, in which d is the actual density and C_p is specific heat capacity calculated by the Dulong–Petit law. The uncertainty of the thermal

conductivity was about 8%, and the uncertainty of ZT was about $20\%^{.35}$

Hall Measurements. The Hall effect was measured for $CdPb_2Bi_4S_9$ and $CdAg_2Bi_6Se_{11}$ at RT with Quantum Design PPMS. Gold wires were attached to the surface of the sample using Dupont 4929N silver paste. The Hall resistivity, $R_{xy} = [R(+H) - R(-H)]/2$, and the carrier density was calculated using the equation $n = 1/[(dR_{xy}/dH)q]$.

Density Functional Theory Calculations. The total energies and relaxed geometries were calculated using density functional theory (DFT) calculations. The generalized gradient approximation of the Perdew–Burke–Ernzerhof exchange–correlation functional with projector augmented wave potentials was applied. We used periodic boundary conditions and a plane-wave basis set, as implemented in the Vienna Ab initio Simulation package. The band structure calculations were performed with spin–orbit coupling to address the heavy species of Pb and Bi. The total energies were numerically converged to approximately 3 meV/cation using a basis set energy cutoff of 500 eV and dense k-meshes corresponding to 4000 k-points per reciprocal atom in the Brillouin zone. In order to perform DFT calculations on materials with mixed atomic occupancy, we used special quasirandom structures. The special quasirandom structures.

Phonon Dispersion Calculations. We employed the Debye–Callaway model to quantitatively evaluate the lattice thermal conductivities. It is well known that the Grüneisen parameters characterize the relationship between phonon frequency and crystal volume change, which allow us to estimate the lattice anharmonicity and to better understand the physical nature of κ_{lat} . The phonon and Grüneisen dispersions were calculated using first-principles DFT phonon calculations within the quasi-harmonic approximation. The phonon dispersions were calculated on a supercell of two volumes, the equilibrium volume V_0 , and the isotropically compressed volume $0.98V_0$.

The Debye–Callaway formalism³⁹ has been demonstrated to produce accurate values of $\kappa_{\rm lat}$ compared with experimental results, especially for low-conductivity TE compounds.^{40,41} $\kappa_{\rm tot}$ can be written as the sum of one longitudinal $\kappa_{\rm LA}$ and two transverse $\kappa_{\rm TA}$ and $\kappa'_{\rm TA}$ acoustic phonon branches: $\kappa_{\rm lat} = \kappa_{\rm LA} + \kappa_{\rm TA} + \kappa_{\rm TA}'$. The partial conductivities $\kappa_{\rm i}$ (i corresponds to TA, TA', and LA modes) are given by

$$\kappa_{i} = \frac{1}{3}C_{i}T^{3} \left\{ \int_{0}^{\Theta_{i}/T} \frac{\tau_{c}^{i}(x)x^{4} e^{x}}{(e^{x} - 1)^{2}} dx + \frac{\left[\int_{0}^{\Theta_{i}/T} \frac{\tau_{c}^{i}(x)x^{4} e^{x}}{\tau_{N}^{i}(e^{x} - 1)^{2}} dx\right]^{2}}{\int_{0}^{\Theta_{i}/T} \frac{\tau_{c}^{i}(x)x^{4} e^{x}}{\tau_{N}^{i}\tau_{U}^{i}(e^{x} - 1)^{2}} dx} \right\}$$

$$(1)$$

Here, Θ_i is the longitudinal (transverse) Debye temperature, $1/\tau_N^i$ is the scattering rate for normal phonon processes, $1/\tau_R^i$ is the sum of all resistive scattering processes, $1/\tau_c^i = 1/\tau_N^i + 1/\tau_R^i$, $x = \hbar\omega/k_BT$, and $C_i = k_B^4/2\pi^2\hbar^3v_i$. \hbar is the Planck constant, k_B is the Boltzmann constant, ω is the phonon frequency, and v_i is the longitudinal or transverse acoustic phonon velocity.

In this case, the resistive scattering rate includes the scattering rates of Umklapp phonon—phonon scattering $(1/\tau_{\rm U}^i)$ and normal phonon scattering $(1/\tau_{\rm N}^i)$. The normal phonon scattering and Umklapp scattering can be expressed as follows

$$\frac{1}{\tau_{\rm N}^{\rm LA}(x)} = \frac{k_{\rm B}^{\,\rm S} \gamma_{\rm LA}^{\,\, 2} V}{M \hbar^4 \nu_{\rm LA}^{\,\, 5}} x^2 T^5 \tag{2}$$

$$\frac{1}{\tau_{\rm N}^{\rm TA/TA'}(x)} = \frac{k_{\rm B}^{\,5} \gamma_{\rm TA/TA'}^{\,2} V}{M \hbar^4 \nu_{\rm TA/TA'}^{\,5}} x T^{\,5}$$
(3)

$$\frac{1}{\tau_{\rm U}^{\rm i}(x)} = \frac{k_{\rm B}^{\ 2} \gamma_{\rm i}^{\ 2}}{M \hbar \nu_{\rm i}^{\ 2} \Theta_{\rm i}} x^2 T^3 \, {\rm e}^{-\theta_{\rm i}/3T} \tag{4}$$

Here, γ , V, and M are the Grüneisen parameter, volume per atom, and average mass of an atom in the crystal, respectively. The Grüneisen

parameter is $\gamma_{\rm i}=-\frac{V\partial\omega_{\rm i}}{\omega_{\rm i}\partial V}$, which characterizes the relationship between the phonon frequency and volume change.

RESULTS AND DISCUSSION

Synthesis and Thermal Behavior. Single crystals of $InPbBi_3S_7$, $In_{0.5}Mn_2Bi_3._5Se_8$, $CdPb_2Bi_4S_9$, $Ag_{1.5}CdBi_5._5Se_{10}$, $Ag_2CdBi_6Se_{11}$, and $Ag_{2.5}Cd_1Sb_{6.5}Se_{12}$ suitable for SCXRD were obtained by slow cooling ($\sim 5~K/h$) from a melted mixture of the respective precursors in a vacuum-sealed tube. The pure phase of $CdPb_2Bi_4S_9$ was obtained by heating a stoichiometric mixture of the elements in a vacuum-sealed fused silica tube to 1273~K followed by annealing at 823~K for 4 days. The pure phase of $CdAg_2Bi_6Se_{11}$ was synthesized by heating a stoichiometric mixture of the elements in a vacuum-sealed fused silica tube to 1273~K followed by water-quenching to RT. The PXRD patterns are presented in Figure 1. All six

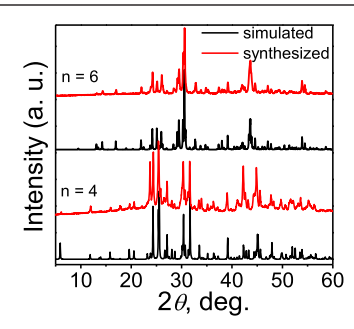


Figure 1. Comparison of PXRD patterns for synthesized CdPb₂Bi₄S₉ (n = 4) and CdAg₂Bi₆Se₁₁ (n = 6) with simulated patterns.

compounds were air-stable and insoluble in water, ethanol, and acetone. Figure S1 presents energy-dispersive X-ray spectroscopy (EDS) spectra and scanning electron microscopy (SEM) images of all the compounds. The EDS elemental analysis results are in good agreement with the crystallographic analysis.

The DTA curves of CdPb₂Bi₄S₉ in Figure 2a reveal three endothermic peaks at 1023, 1050, and 1096 K, which correspond to the decomposition of CdPb₂Bi₄S₉ and melting of the decomposed compounds. Upon cooling, three exothermic peaks appeared at 1012, 1031, and 1068 K, which correspond to the crystallization of the decomposed products and residual CdPb₂Bi₄S₉. The PXRD pattern of the

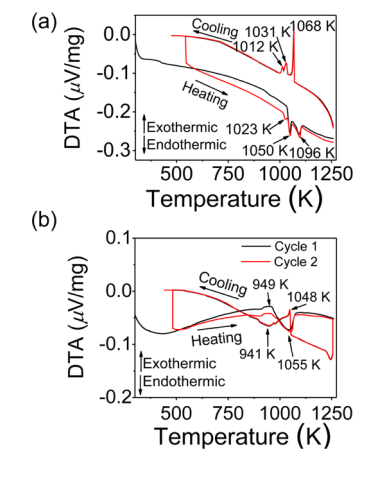


Figure 2. DTA curves for (a) CdPb₂Bi₄S₉ and (b) CdAg₂Bi₆Se₁₁.

Table 1. Crystal Data and Structure Refinements for $M_{n+1}(Bi/Sb)_2Q_{n+5}$ at 293(2) K^{α}

$M_{n+1}(Bi/Sb)_2Q_{n+5}$	n = 2	n = 3	n = 4	n = 5	<i>9</i> = <i>u</i>	n = 7
empirical formula	$InPbBi_3S_7$	$\mathrm{In}_{0.5}\mathrm{Mn}_2\mathrm{Bi}_{3.5}\mathrm{Se}_8$	$CdPb_2Bi_4S_9$	$\mathrm{Ag}_{1.5}\mathrm{CdBi}_{5.5}\mathrm{Se}_{10}$	$Ag_2CdBi_6Se_{11}$	$Ag_{2.5}Cd_1Sb_{6.5}Se_{12}$
formula weight	1173.37	1529.59	1651.24	2208.86	2450.58	2103.88
temperature	293(2) K					
wavelength	0.71069 Å					
crystal system	monoclinic					
space group	C2/m					
unit cell dimensions	a = 13.014(4) Å, b = 3.9911(10) Å, $c = 12.003(3) \text{ Å}, \alpha = 90^{\circ},$ $\beta = 104.23(2)^{\circ}, \gamma = 90^{\circ}$	a = 13.279(3) Å, b = 4.0662(8)Å, $c = 14.988(3)\text{Å}, \alpha = 90^{\circ},$ $\beta = 115.43(3)^{\circ}, \gamma = 90^{\circ}$	a = 13.159(3) Å, b = 4.0100(8) Å, $c = 15.145(3) \text{ Å}, \alpha = 90.00^{\circ},$ $\beta = 99.82(3), \gamma = 90.00^{\circ}$	a = 13.679(8) Å, b = 4.1552(19) Å, $c = 17.097(9) \text{ Å}, \alpha = 90^{\circ},$ $\beta = 93.53(3)^{\circ}, \gamma = 90^{\circ}$	a = 13.633(3) Å, b = 4.1461(8)Å, $c = 19.335(4)$ Å, $\alpha = 90^{\circ}$, $\beta = 104.64(3)^{\circ}$, $\gamma = 90^{\circ}$	a = 13.547(3) Å, b = 4.0870(8) Å, $c = 20.706(4) \text{ Å}, \alpha = 90^{\circ},$ $\beta = 102.36(3)^{\circ}, \gamma = 90^{\circ}$
volume $(Å^3)$	604.3(3)	730.9(3)	787.5(3)	970.0(9)	1057.4(4)	1119.8(4)
Z	2	2	2	2	2	2
density (calculated) (g/cm^3)	6.449	6.950	6.963	7.564	7.696	6.239
absorption coefficient (mm^{-1})	60.455	64.123	68.303	70.677	71.438	30.129
F(000)	984	1274	1376	1827	2028	1795
heta range for data collection	3.23°-24.99°	3.01°-25.00°	3.14°-25.00°	1.19°-24.99°	2.18°-33.37°	$3.02^{\circ} - 29.11^{\circ}$
Index ranges	$-15 \le h \le 15, -4 \le k \le 4,$ $-14 \le l \le 12$	$-15 \le h \le 14, -4 \le k \le 4,$ $-17 \le l \le 17$	$-15 \le h \le 15, -4 \le k \le 4,$ $-18 \le l \le 17$	$-16 \le h \le 16, -4 \le k \le 4,$ $-19 \le l \le 20$	$-20 \le h \le 20, -5 \le k \le 6,$ $-29 \le l \le 29$	$-18 \le h \le 18, -5 \le k \le 5,$ $-28 \le l \le 28$
reflections collected	4638	2400	1867	5567	7179	5376
independent reflections	$604 [R_{int} = 0.0362]$	743 $[R_{int} = 0.1271]$	$777 [R_{int} = 0.0439]$	$964 [R_{int} = 0.0456]$	$2121 \left[R_{\rm int} = 0.1289 \right]$	$1712 [R_{int} = 0.0854]$
completeness to $\theta = 24.991^{\circ}$	98.2%	99.3%	%8'96	%9'86	92.3%	%9.66
refinement method	full-matrix least-squares on ${\it F}^{2}$					
data/restraints/parameters	604/0/39	743/0/46	777/0/51	964/0/58	2121/0/64	1712/0/71
goodness-of-fit	1.095	0.827	1.052	1.172	0.741	1.035
final R indices $[I>2\sigma(\mathrm{I})]$	$R_1 = 0.0342$, w $R_1 = 0.0983$	$R_1 = 0.0727$, $wR_1 = 0.1804$	$R_1 = 0.0544$, $wR_1 = 0.1287$	$R_1 = 0.0267$, $wR_1 = 0.0812$	$R_1 = 0.0595$, w $R_1 = 0.1331$	$R_1 = 0.0477$, w $R_1 = 0.1248$
R indices [all data]	$R_2 = 0.0345$, w $R_2 = 0.0986$	$R_2 = 0.0783$, w $R_2 = 0.1908$	$R_2 = 0.0656$, w $R_2 = 0.1345$	$R_2 = 0.0310$, $wR_2 = 0.0893$	$R_2 = 0.1345$, w $R_2 = 0.1572$	$R_2 = 0.0643$, w $R_2 = 0.1324$
$^{a}R = \sum F_{o} - F_{c} /\sum F_{o} $	Taggest unit. peak and note 5.500 and 2.500 erg. $^{+.5+5}$ and $^{-5.012}$ erg $^{-6}R = \sum I F_0 - F_0 /\sum F_0 , \text{wR} = \{\sum [\text{w}(F_0 ^2 - F_0 ^2)^2]/\sum [\text{w}(F_0 ^4)]\}^{1/2},$	$[1/2] = \frac{1.343 \text{ and } -3.012 \text{ erg}}{[1/2] [1/2] [1/2]}$ and w = 1	and w = $1/[\sigma^2(F_o^2) + (0.1000P)^2]$, where $P = (F_o^2 + 2F_c^2)/3$.	ere $P = (F_0^2 + 2F_c^2)/3$.	7.501 dild=4.303 e.A	2.402 diu = 5.154 e.A

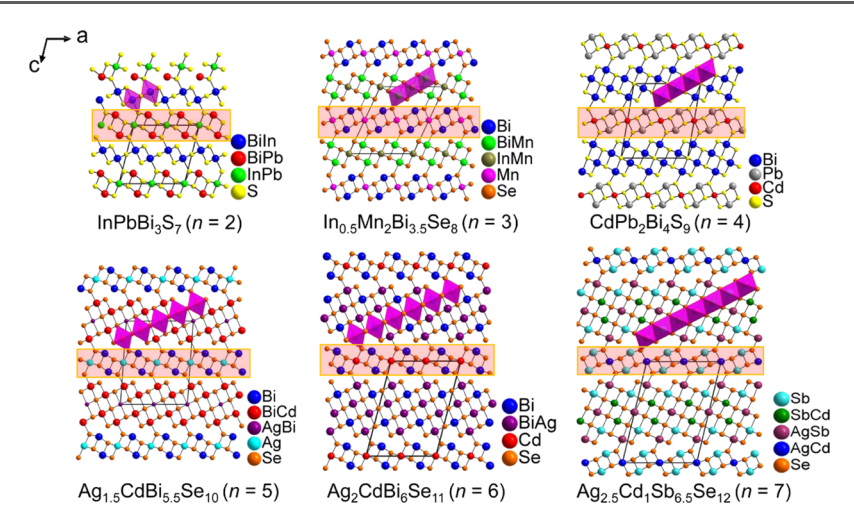


Figure 3. Homologous sequence of pavonite structures with different numbers of octahedra along the diagonal of the "accreting" galena slab.

DTA product in Figure S2a confirms incongruent melting of CdPb₂Bi₄S₉ with peaks of undecomposed CdPb₂Bi₄S₉ still remaining. Upon heating CdAg₂Bi₆Se₁₁, an exothermic peak appears at 949 K, which corresponds to the decomposition, and an endothermic peak appears at 1055 K, which corresponds to melting. Upon cooling CdAg₂Bi₆Se₁₁, an exothermic peak appears at 1048 K, corresponding to the crystallization of the undecomposed CdAg₂Bi₆Se₁₁, and an endothermic peak appears at 941 K, as shown in Figure 2b. The two consecutive heating—cooling cycles in the DTA curve agree well with one another. The PXRD pattern of the DTA product in Figure S2b shows that CdAg₂Bi₆Se₁₁ starts to decompose before melting; however, diffraction peaks of the undecomposed sample still remain.

Crystal Structure. All the compounds crystallized in the C2/m space group, and Table 1 provides the refinement details and the unit cell parameters of the crystal structures. All the compounds belong to the pavonite homology with the general chemical formula of $M_{n+1}(Bi/Sb)_2Q_{n+5}$, where n varies from 2 to 7 (Figure 3). The homologous crystal structures consist of two alternating slabs that stack perpendicular to the c-axis. One of the slabs is usually referred to as a "accreting" slab with different widths containing different numbers (n) of octahedra along the diagonal direction; ⁴² this slab can be regarded as an adjustable block excised from a cubic NaCl lattice (or galenatype structure) perpendicular to the [311] direction. ^{22,43} The other slab is referred to as a "non-accreting" slab consisting of a pair of square pyramidal columns of MQ_s , interconnected by an octahedral column MQ_6 (M = Ag, Cd, In, Mn, or Pb; Q = S or Se).

In the six new structures reported here, Pb and Bi (or Sb) can be completely mixed to occupy same lattice sites. The Mn, Ag, and Cd atoms can also share positions with Pb and Bi (or Sb) because of the high tolerance of these crystallographic sites for different sized atoms. ^{20,44} Detailed information on the atomic occupancy, coordination number, and bond length of these compounds can be found in Table S1. In nature, the common cations of this series of mineral sulfosalts are Bi, Ag, Cu, or Pb; in some cases, divalent Pb can be replaced by Cd, Hg, or Mn, and in more rare cases, Se can also replace S. ^{28,45,46} The n values of this series range from 0 to 8; examples for n = 0 are AgBiSCl₂ and CuBiSCl₂, ⁴⁷ and an example for n = 8 is Ag_{3.5}Bi_{7.5}S₁₃. ⁴⁸ Halogen members of this series can be obtained by substituting some of the sulfur atoms with the univalent

anions Cl, Br, or I. 48,49 This halogen substitution approach has also been demonstrated to be an effective means of designing new structures, as reported for the pavonite series with n=1,2,3,4,5, and 7 compounds in the Ag–Bi–S–Cl (or –Br) system. 20,50 Notably, the n=6 member is conspicuously rare, both among minerals and synthetic compounds, with only ${\rm Ag_5Bi_{13}S_{22}}$ (n=6) being structurally analyzed. 27 Thus, the stabilization of ${\rm Ag_2CdBi_6Se_{11}}$ (n=6) in this contribution is particularly interesting.

Optical Measurements and Electronic Structure Calculations. $CdPb_2Bi_4S_9$ is a semiconductor with an optical band gap of 1.0 eV, Figure S3a. The band gap of $CdAg_2Bi_6Se_{11}$ is much narrower at $\sim 0.05 \text{ eV}$, as shown in Figure S3b. First-principles electronic structure calculations indicate that both $CdPb_2Bi_4S_9$ and $CdAg_2Bi_6Se_{11}$ are indirect-band-gap semiconductors, as shown in Figure 4a,b. The calculated band gaps

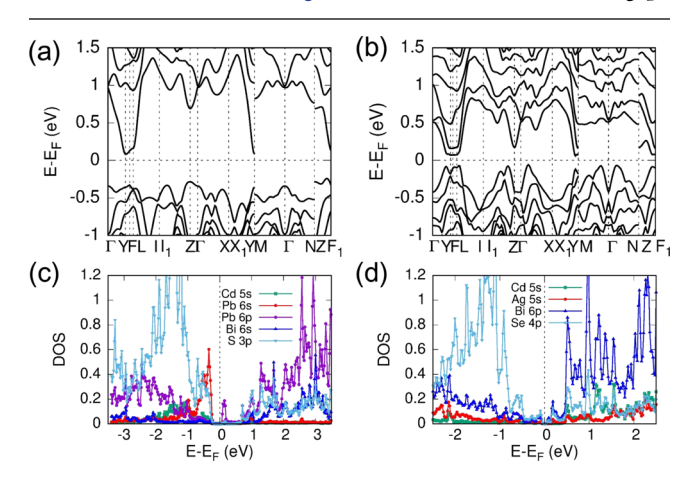


Figure 4. (a, b) Electronic band structure of $CdPb_2Bi_4S_9$ and $CdAg_2Bi_6Se_{11}$. (c, d) Partial density of states of $CdPb_2Bi_4S_9$ and $CdAg_2Bi_6Se_{11}$.

of $CdPb_2Bi_4S_9$ and $CdAg_2Bi_6Se_{11}$ are 0.39 and 0.09 eV, respectively. The projected electronic density of states for $CdPb_2Bi_4S_9$ indicates that the valence band maximum is mainly contributed from Pb 6s and S 3p states and that the conduction band minimum is from Pb 6p states, as shown in Figure 4c. The contribution of the Cd states to the conduction band minimum is negligible, suggesting that electron transport in this material occurs mainly through Pb-based 6p orbitals.

For CdAg₂Bi₆Se₁₁, the valence band top consists mainly of Se 4p states and the conduction band bottom consists mainly of Bi 6p and Se 4p states, as shown in Figure 4d.

Charge Transport Properties. Dense pellets of CdPb₂Bi₄S₉ and CdAg₂Bi₆Se₁₁ were prepared using SPS. Figure 5 presents photographs and SEM images of the freshly

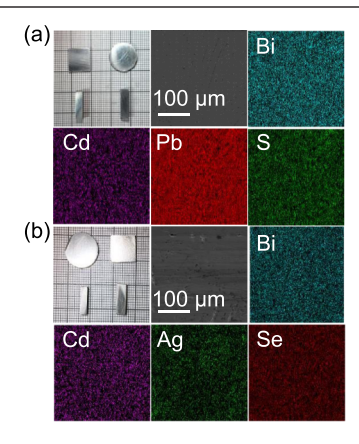


Figure 5. Photographs, SEM images, and EDS elemental mapping of freshly polished surfaces of SPS-processed (a) CdPb₂Bi₄S₉ and (b) CdAg₂Bi₆Se₁₁.

polished surfaces of the specimens. EDS mapping revealed that all the elements were homogenously dispersed. The electrical conductivity and Seebeck coefficients were measured perpendicular to the SPS pressure direction. For the CdPb₂Bi₄S₉ samples, the electrical conductivity was ~79 S·cm⁻¹ at 300 K and decreased monotonically with increasing temperature to ~36 S·cm⁻¹ at 810 K, as shown in Figure 6a. The carrier concentration for CdPb₂Bi₄S₉ derived from Hall effect measurements was ~1.6 \times 10¹⁸ cm⁻³ at RT with electrons being the dominant carrier, Figure S5.

 $CdAg_2Bi_6Se_{11}$ also behaved like a doped semiconductor with an electrical conductivity of ~267 S·cm⁻¹ at 325 K, as shown in Figure 6. The electrical conductivity slowly decreasing with temperature increasing till 550 K and then increasing with temperature rising. The carrier concentration derived from Hall effect measurements was 1.8×10^{19} cm⁻³ at RT with electrons being the dominant carrier, Figure S6. $CdAg_2Bi_6Se_{11}$

possesses the highest electrical conductivity among reported pavonites; for example, $\mathrm{Mn_{1.34}Sn_{6.66}Bi_8Se_{20}}$ (n=5)²⁵ and $\mathrm{InSn_2Bi_3Se_8}$ (n=3)⁵¹ have electrical conductivities of 47 and 79 S·cm⁻¹ at RT, respectively; CdPbBi₄Se₈ (n=3) exhibited an electrical conductivity of 78 S·cm⁻¹ at 320 K; CdSnBi₄Se₈ (n=3) exhibited an electrical conductivity of 150 S·cm⁻¹ at 320 K;²⁴ and LiSn₂Bi₅S₁₀ (n=5) behaved as a doped n-type semiconductor with an electrical conductivity of approximately 165 S·cm⁻¹ at RT.²⁰

As shown in Figure 6d, κ_{tot} for both CdPb₂Bi₄S₉ and CdAg₂Bi₆Se₁₁ was extremely low, with values of 0.78 and 0.54 W·m⁻¹·K⁻¹ at 300 K, respectively. These values decreased with increasing temperature to 0.52 and 0.40 W·m⁻¹·K⁻¹ at 765 K, respectively. A small rise in the thermal conductivity was observed for both compounds above 765 K, which is attributed to bipolar conduction. These values are comparable to the reported thermal conductivities of other pavonites, for example, 0.6, 0.6, 0.64, 0.69, and 0.8 W·m⁻¹·K⁻¹ for AgBi₃S₅ (n = 5), ⁵² Mn_{1.34}Sn_{6.66}Bi₈Se₂₀ (n = 5), CdPbBi₄Se₈ (n = 3), ²⁴ $CdSnBi_4Se_8$ $(n = 3)^{24}$ and $LiSn_2Bi_5S_{10}$ $(n = 5)^{20}$ at RT, respectively. κ_{tot} is composed of an electronic-conducting contribution (κ_{ele}) and lattice-conducting contribution (κ_{lat}). The electronic thermal conductivity can be calculated using the equation $\kappa_{\rm ele} = L\sigma T$, which is called the Wiedemann-Franz law. κ_{lat} is obtained by subtracting the electronic part from the total thermal conductivity. The Lorenz number L (Figure S4a)

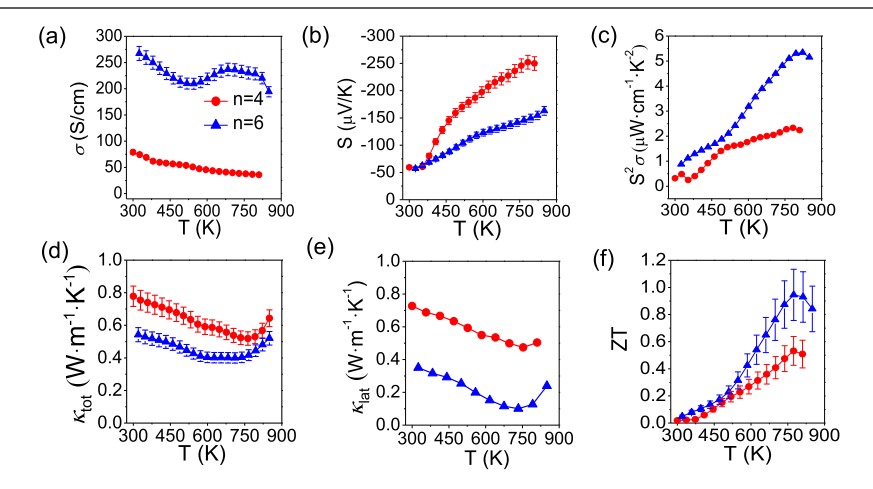


Figure 6. Temperature dependence of TE properties of $CdPb_2Bi_4S_9$ (n=4, red lines) and $CdAg_2Bi_6Se_{11}$ (n=6, blue lines): (a) electrical conductivity, (b) Seebeck coefficient, (c) PF, (d) total thermal conductivity, (e) lattice thermal conductivity, and (f) figure of merit. All the data were measured perpendicular to the SPS pressure direction.

was calculated with the assumptions of the acoustic-phonon scattering mechanism and a single-parabolic-band mode by fitting the Seebeck coefficient using the following equations⁵⁷

$$S = \pm \frac{k_{\rm B}}{e} \left[\eta - \frac{2F_{\rm I}(\eta)}{F_{\rm 0}(\eta)} \right] \tag{5}$$

$$L = \left(\frac{k_{\rm B}}{e}\right)^2 \left\{ \frac{3F_2(\eta)}{F_0(\eta)} - \left[\frac{2F_1(\eta)}{F_0(\eta)}\right]^2 \right\}$$
 (6)

$$F_{j}(\eta) = \int_{0}^{\infty} \frac{x^{j}}{e^{(x-\eta)} + 1} dx$$
 (7)

Here, $k_{\rm B}$ is the Boltzmann constant and $F_{\rm i}(\eta)$ is the Fermi integral calculated from the reduced Fermi level, $\eta = E_{\rm F}/k_{\rm B}T$. As observed in Figure 6e, κ_{lat} of CdPb₂Bi₄S₉ was at the same level as κ_{tot} because the low electrical conductivity resulted in a negligible electronic thermal conductivity contribution. More specifically, κ_{lat} of CdPb₂Bi₄S₉ decreased from 0.73 W·m⁻¹·K⁻¹ at 325 K to 0.5 W·m⁻¹·K⁻¹ at 810 K. κ_{lat} of CdAg₂Bi₆Se₁₁ was ultralow ~0.35 W·m⁻¹·K⁻¹ at 325 K and decreased further to 0.1 W·m⁻¹·K⁻¹ at 733 K. Such low lattice thermal conductivity values for CdAg₂Bi₆Se₁₁ are attributed to its complex structure, the mixed site occupancy resulting in intrinsic mass contrast, and the relatively large unit cell volume of 1119.8(4) $Å^3$. These factors are further discussed in the theoretical calculations section. The κ_{lat} values of CdAg₂Bi₆Se₁₁ are comparable to those of some state-of-the-art TE materials with low lattice thermal conductivities, for example, Cu_{2-x} Se with $\kappa_{lat} \approx 0.4$ – 0.6 W·m⁻¹·K⁻¹ over the entire temperature range, ⁵⁸ SnSe single crystal with the lowest $\kappa_{\rm lat}$ value of 0.20 W·m⁻¹·K⁻¹ along the *a* direction at 973 K, ⁵⁹⁻⁶¹ CsAg₅Te₃ with the lowest $\kappa_{\rm lat}$ value of 0.14 W·m⁻¹·K⁻¹ at 727 K,⁶² Tl₃VSe₄ with $\kappa_{\rm lat} \approx$ $0.30 \text{ W} \cdot \text{m}^{-1} \cdot \text{K}^{-1}$ at 300 K, 63 AgCuTe with κ_{lat} between 0.2 and 0.4 W·m⁻¹·K⁻¹, 64 and Tl₂Ag₁₂Te_{7+ δ} with κ_{lat} varies between $0.20 \text{ W} \cdot \text{m}^{-1} \cdot \text{K}^{-1}$ and $0.25 \text{ W} \cdot \text{m}^{-1} \cdot \text{K}^{-1}$ from RT to 525 K.⁶⁵

The ZT values calculated using the above transport properties are presented in Figure 7f. For CdPb₂Bi₄S₉ and CdAg₂Bi₆Se₁₁, the highest ZT values of 0.53 and 0.95, respectively, were obtained at 775 K. The ZT value of CdAg₂Bi₆Se₁₁ is comparable to that of undoped PbTe, which was reported to be 0.8–1.0 at approximately 650 K⁶⁶ and 0.8 at 700 K.⁶⁷ All these results indicate that both of these compounds are good candidates for further doping studies, band gap engineering, and nanostructuring to further improve the TE properties.

Generally, the average low κ_{lat} of CdPb₂Bi₄S₉ originates from the very low phonon velocities. Therefore, DFT-based phonon calculations were carried out to elucidate the acoustic phonon modes which define to a larger extend the thermal conductivity. The phonon velocities can be calculated from the slope of the acoustic phonon dispersion around the Γ point in Figure 7a; average phonon velocities of 1457, 1714, and 2925 m/s were determined for the TA, TA', and LA modes, respectively. The phonon density of states indicates that acoustic phonon transport in phonon velocities is primarily based on the motions of the heavier Bi atoms with minimal contribution from S. The averaged Grüneisen parameters were relatively large with values of 2.62, 2.46, and 3.08 for the TA, TA' and LA mode contributions, respectively, as shown in Figure 7b. Finally, as shown in Figure 7c, the theoretically calculated CdPb₂Bi₄S₉ lattice thermal conductivities in the a

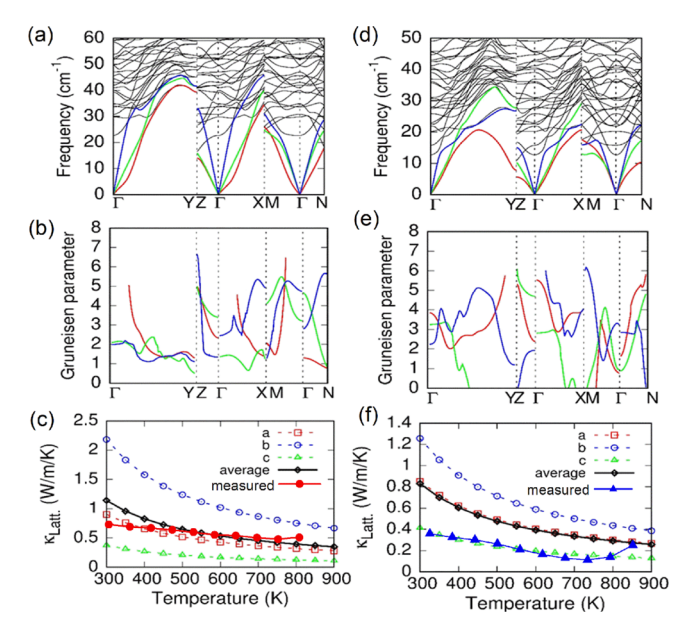


Figure 7. Calculated (a) phonon dispersion, (b) Grüneisen parameters, and (c) lattice thermal conductivity of $CdPb_2Bi_4S_9$. The red, green, and blue lines denote the TA, TA', and LA acoustic modes, respectively. Comparison of calculated and measured properties for $CdAg_2Bi_6Se_{11}$: (d) phonon dispersion, (e) Grüneisen parameters, and (f) lattice thermal conductivity.

and c directions were as low as ~ 0.9 and $0.4 \text{ W} \cdot \text{m}^{-1} \cdot \text{K}^{-1}$, respectively, at 300 K. For the b (4.01 Å) direction, the relatively shorter lattice dimension than a (13.159 Å) and c (15.14 Å) induced relatively larger Debye temperatures and hence a higher κ_{lat} of 2.5 W·m⁻¹·K⁻¹ at 300 K. We considered the average of the calculated κ_{lat} values for the three lattice directions based on the monoclinic Brillouin zone. A comparison between the calculated values and the experimental observations is shown in Figure 7c. The calculated values gradually decreased from 1.2 to 0.4 W·m⁻¹·K⁻¹ in the range of 300-900 K. The values close to RT are higher than the experimental results; however, at high temperatures, they agree well with the experimental values. The higher average calculated values of κ_{lat} close to RT are due to the fact that we only considered normal acoustic phonons and Umklapp scattering processes. Other phonon-scattering mechanisms may exist in actual samples, such as defects, cation disorders, and grain boundary contributions, which are not considered in our calculations.

The averaged calculated phonon velocities for CdAg₂Bi₆Se₁₁ were obtained from Figure 7d: 1284, 1545, and 2654 m/s for the TA, TA', and LA modes, respectively, which are all lower than the values calculated for CdPb2Bi4S9, thus leading to lower κ_{lat} . As observed in Figure 7e, the averaged Grüneisen parameters for CdAg₂Bi₆Se₁₁ were 2.60, 2.34, and 2.98 for the TA, TA', and LA branches, respectively, which differ slightly from those of CdPb₂Bi₄S₉. As observed in Figure 7f, the lattice thermal conductivities of CdAg₂Bi₆Se₁₁ were lower than those of CdPb₂Bi₄S₉; the average atomic mass of CdAg₂Bi₆Se₁₁ is ~18% greater than that of CdPb₂Bi₄S₉, which induces lower acoustic and vibrational frequencies for CdAg₂Bi₆Se₁₁. However, the calculated lattice thermal conductivities of CdAg₂Bi₆Se₁₁ were higher than the measured values, as the crystal structure model used for the calculation did not account for many other phonon-scattering mechanisms such as grain

boundary contributions, defects, and so forth. In general, the calculated $\kappa_{\rm lat}$ values for both CdPb₂Bi₄S₉ and CdAg₂Bi₆Se₁₁ are very low because the complex atomic structure induces lower Debye temperatures, slow phonon velocities, and large Grüneisen parameters.

CONCLUDING REMARKS

Six new compounds belonging to the pavonite homologous series with a general formula of $\mathrm{M_{n+1}(Bi/Sb)_2Q_{n+5}}$ were obtained with n varying from 2 to 7, including $\mathrm{InPbBi_3S_7}$ (n=2), $\mathrm{In_{0.5}Mn_2Bi_{3.5}Se_8}$ (n=3), $\mathrm{CdPb_2Bi_4S_9}$ (n=4), $\mathrm{Ag_{1.5}CdBi_{5.5}Se_{10}}$ (n=5), $\mathrm{Ag_2CdBi_6Se_{11}}$ (n=6), and $\mathrm{Ag_{2.5}CdSb_{6.5}Se_{12}}$ (n=7). These materials are indirect-gap n-type semiconductors. κ_{lat} of $\mathrm{CdPb_2Bi_4S_9}$ was very low (less than 0.73 W·m $^{-1}$ ·K $^{-1}$) in the temperature range of 325–810 K, and $\mathrm{CdAg_2Bi_6Se_{11}}$ exhibited ultralow κ_{lat} of 0.35 W·m $^{-1}$ ·K $^{-1}$ at 325 K and 0.1 W·m $^{-1}$ ·K $^{-1}$ at 733 K. Theoretical calculations revealed the origins of these low κ_{lat} values to be the low Debye temperature, slow phonon velocities, and large Grüneisen parameters. As a result, the highest ZT values of 0.53 and 0.95 were obtained for $\mathrm{CdPb_2Bi_4S_9}$ and $\mathrm{CdAg_2Bi_6Se_{11}}$ at 775 K, respectively. This series of compounds are potentially excellent TE materials and deserve further investigation.

ASSOCIATED CONTENT

Supporting Information

The Supporting Information is available free of charge on the ACS Publications website at DOI: 10.1021/acs.chemmater.9b00585.

Experiments; tables of atomic coordinates, displacement parameters, anisotropic displacement parameters, and bond distances of all these compounds; SEM images and EDS spectra of all these compounds; PXRD patterns of DTA products of CdPb₂Bi₄S₉ and Ag₂CdBi₆Se₁₁; UV—vis and FT-IR spectra; Lorenz number obtained by fitting Seebeck coefficients and thermal diffusivity of CdPb₂Bi₄S₉ and Ag₂CdBi₆Se₁₁; and magnetic-field dependence of Hall resistivity of the samples (PDF) X-ray crystallographic data of In_{0.5}Mn₂Bi_{3.5}Se₈ (CIF) X-ray crystallographic data of CdPb₂Bi₄S₉ (CIF) X-ray crystallographic data of Ag_{1.5}CdBi_{5.5}Se₁₀ (CIF) X-ray crystallographic data of Ag_{2.5}CdBi_{6.5}Se₁₀ (CIF) X-ray crystallographic data of Ag_{2.5}CdBi_{6.5}Se₁₁ (CIF)

X-ray crystallographic data of Ag_{2.5}Cd₁Sb_{6.5}Se₁₂ (CIF)

AUTHOR INFORMATION

Corresponding Author

*E-mail: m-kanatzidis@northwestern.edu.

ORCID ®

Jing Zhao: 0000-0002-8000-5973 Saiful M. Islam: 0000-0001-8518-1856 Haijie Chen: 0000-0003-3567-1763 Shulan Ma: 0000-0002-8326-3134

Christopher Wolverton: 0000-0003-2248-474X Mercouri G. Kanatzidis: 0000-0003-2037-4168

Notes

The authors declare no competing financial interest.

ACKNOWLEDGMENTS

This work was supported mainly by the National Science Foundation grant DMR-1708254. This work was also supported by Beijing Municipal Natural Science Foundation, China (2182080, 2182029) and Grant from the National Natural Science Foundation of China (51702329 and 51832005). This work made use of the EPIC facility (NUANCE Center-Northwestern University), which has received support under the State of Illinois, Northwestern University, and the National Science Foundation with Grants DMR-1720139 through the MRSEC program at the Materials Research Center, and EEC-0118025/003 through The Nanoscale Science and Engineering Center. S.H. and C.W.(DFT calculations) acknowledge support from the Department of Energy, Office of Science Basic Energy Sciences under Grant DE-SC0014520. Access of QUEST, the supercomputing resources facilities at Northwestern University is acknowledged.

REFERENCES

- (1) Kanatzidis, M. G. Discovery-Synthesis, Design, and Prediction of Chalcogenide Phases. *Inorg. Chem.* **2017**, *56*, 3158–3173.
- (2) Tang, G.; Wei, W.; Zhang, J.; Li, Y.; Wang, X.; Xu, G.; Chang, C.; Wang, Z.; Du, Y.; Zhao, L.-D. Realizing High Figure of Merit in Phase-Separated Polycrystalline Sn_{1-x}Pb_xSe. *J. Am. Chem. Soc.* **2016**, 138, 13647–13654.
- (3) Zhao, L.-D.; Chang, C.; Tan, G.; Kanatzidis, M. G. SnSe: a Remarkable New Thermoelectric Material. *Energy Environ. Sci.* **2016**, 9, 3044–3060.
- (4) Korkosz, R. J.; Chasapis, T. C.; Lo, S.-h.; Doak, J. W.; Kim, Y. J.; Wu, C.-I.; Hatzikraniotis, E.; Hogan, T. P.; Seidman, D. N.; Wolverton, C.; Dravid, V. P.; Kanatzidis, M. G. High ZT in p-Type $(PbTe)_{1-2x}(PbSe)_x(PbS)_x$ Thermoelectric Materials. *J. Am. Chem. Soc.* **2014**, *136*, 3225–3237.
- (5) He, J.; Blum, I. D.; Wang, H.-Q.; Girard, S. N.; Doak, J.; Zhao, L.-D.; Zheng, J.-C.; Casillas, G.; Wolverton, C.; Jose-Yacaman, M.; Seidman, D. N.; Kanatzidis, M. G.; Dravid, V. P. Morphology Control of Nanostructures: Na-Doped PbTe-PbS System. *Nano Lett.* **2012**, *12*, 5979–5984.
- (6) He, J.; Girard, S. N.; Zheng, J.-C.; Zhao, L.; Kanatzidis, M. G.; Dravid, V. P. Strong Phonon Scattering by Layer Structured PbSnS₂ in PbTe Based Thermoelectric Materials. *Adv. Mater.* **2012**, *24*, 4440–4444
- (7) Chatterjee, A.; Biswas, K. Solution-Based Synthesis of Layered Intergrowth Compounds of the Homologous Pb_mBi_{2n}Te_{3n+m} Series as Nanosheets. *Angew. Chem., Int. Ed.* **2015**, *54*, 5623–5627.
- (8) Imai, Y.; Watanabe, A. Electronic Structures of PbBi₄Te₇ and GeBi₄Te₇ Calculated by a First-Principle Pseudopotential Method. *Intermetallics* **2003**, *11*, 451–458.
- (9) Kuropatwa, B. A.; Kleinke, H. Thermoelectric Properties of Stoichiometric Compounds in The $(SnTe)_x(Bi_2Te_3)_y$ System. *Z. Anorg. Allg. Chem.* **2012**, 638, 2640–2647.
- (10) Sasaki, S.; Segawa, K.; Ando, Y. Superconductor Derived from a Topological Insulator Heterostructure. *Phys. Rev. B: Condens. Matter Mater. Phys.* **2014**, *90*, 220504.
- (11) Sassi, S.; Candolfi, C.; Delaizir, G.; Migot, S.; Ghanbaja, J.; Gendarme, C.; Dauscher, A.; Malaman, B.; Lenoir, B. Crystal Structure and Transport Properties of the Homologous Compounds $(PbSe)_5(Bi_2Se_3)_{3m}$ (m=2,3). *Inorg. Chem.* **2018**, *57*, 422–434.
- (12) Momida, H.; Bihlmayer, G.; Blügel, S.; Segawa, K.; Ando, Y.; Oguchi, T. Topological Interface States in the Natural Heterostructure (PbSe)₅(Bi₂Se₃)₆ with BiPb Defects. *Phys. Rev. B* **2018**, 97, 035113.
- (13) Kanatzidis, M. G. Structural Evolution and Phase Homologies for "Design" and Prediction of Solid-State Compounds. *Acc. Chem. Res.* **2005**, *38*, 359–368.
- (14) Hsu, K.-F.; Lal, S.; Hogan, T.; Kanatzidis, M. G. CsPb₃Bi₃Te₈ and CsPb₄Bi₃Te₉: Low-Dimensional Compounds and the Homologous Series CsPb_mBi₃Te_{5+m}. *Chem. Commun.* **2002**, 1380–1381.

(15) Ruck, M.; Poudeu Poudeu, P. F. Homologous Silver Bismuth Chalcogenide Halides ${}^{(N, x)}$ P. III. The ${}^{(4, x)}$ P, ${}^{(5, x)}$ P, and ${}^{(7, x)}$ P Structure Families of Modular Compounds with Tunable Composition and Structure. *Z. Anorg. Allg. Chem.* **2008**, 634, 482–490.

- (16) Stoumpos, C. C.; Cao, D. H.; Clark, D. J.; Young, J.; Rondinelli, J. M.; Jang, J. I.; Hupp, J. T.; Kanatzidis, M. G. Ruddlesden-Popper Hybrid Lead Iodide Perovskite 2D Homologous Semiconductors. *Chem. Mater.* **2016**, *28*, 2852–2867.
- (17) Ohta, M.; Chung, D. Y.; Kunii, M.; Kanatzidis, M. G. Low Lattice Thermal Conductivity in Pb₅Bi₆Se₁₄, Pb₃Bi₂S₆, and PbBi₂S₄: Promising Thermoelectric Materials in the Cannizzarite, Lillianite, and Galenobismuthite Homologous Series. *J. Mater. Chem. A* **2014**, *2*, 20048–20058.
- (18) Casamento, J.; Lopez, J. S.; Moroz, N. A.; Olvera, A.; Djieutedjeu, H.; Page, A.; Uher, C.; Poudeu, P. F. P. Crystal Structure and Thermoelectric Properties of the ^{7,7}L Lillianite Homologue Pb₆Bi₂Se₉. *Inorg. Chem.* **2017**, *56*, 261–268.
- (19) Olvera, A.; Shi, G.; Djieutedjeu, H.; Page, A.; Uher, C.; Kioupakis, E.; Poudeu, P. F. P. Pb₇Bi₄Se₁₃: A Lillianite Homologue with Promising Thermoelectric Properties. *Inorg. Chem.* **2015**, *54*, 746–755
- (20) Khoury, J. F.; Hao, S.; Stoumpos, C. C.; Yao, Z.; Malliakas, C. D.; Aydemir, U.; Slade, T. J.; Snyder, G. J.; Wolverton, C.; Kanatzidis, M. G. Quaternary Pavonites $A_{1+x}Sn_{2-x}Bi_{5+x}S_{10}$ ($A^+ = Li^+$, Na^+): Site Occupancy Disorder Defines Electronic Structure. *Inorg. Chem.* **2018**, 57, 2260–2268.
- (21) Qin, B.-C.; Xiao, Y.; Zhou, Y.-M.; Zhao, L.-D. Thermoelectric transport properties of Pb-Sn-Te-Se system. *Rare Met.* **2017**, *37*, 343–350.
- (22) Makovicky, E.; Mumme, W. G.; Watts, J. A. The Crystal Structure of Synthetic Pavonite, AgBi₃S₅, and the Definition of the Pavonite Homologous Series. *Can. Mineral.* 1977, *15*, 339–348.
- (23) Perez-Mato, J. M.; Elcoro, L.; Makovicky, E.; Topa, D.; Petříček, V.; Madariaga, G. Conspicuous Variation of the Lattice Unit Cell in the Pavonite Homologous Series and its Relation with Cation/Anion Occupational Modulations. *Mater. Res. Bull.* **2013**, 48, 2166–2174
- (24) Zhao, J.; Islam, S. M.; Hao, S.; Tan, G.; Su, X.; Chen, H.; Lin, W.; Li, R.; Wolverton, C.; Kanatzidis, M. G. Semiconducting Pavonites $CdMBi_4Se_8$ (M=Sn and Pb) and Their Thermoelectric Properties. *Chem. Mater.* **2017**, *29*, 8494–8503.
- (25) Anglin, C.; Takas, N.; Callejas, J.; Poudeu, P. F. P. Crystal Structure and Physical Properties of the Quaternary Manganese-Bearing Pavonite Homologue Mn_{1.34}Sn_{6.66}Bi₈Se₂₀. J. Solid State Chem. **2010**, 183, 1529–1535.
- (26) Ahn, J. Y.; Hwang, J.-Y.; Ryu, B. K.; Oh, M.-W.; Lee, K. H.; Kim, S. W. Importance of Crystal Chemistry with Interstitial Site Determining Thermoelectric Transport Properties in Pavonite Homologue Cu-Bi-S Compounds. *CrystEngComm* **2016**, *18*, 1453–1461.
- (27) Makovicky, E.; Paar, W. H.; Putz, H.; Zagler, G. Ag₅Bi₁₃S₂₂, the P-6 Natural Member of the Pavonite Homologous Series, from Erzwies, Austria. *Can. Mineral.* **2010**, *48*, 467–481.
- (28) Chaplygin, I. V.; Mozgova, N. N.; Magazina, L. O.; Kuznetsova, O. Y.; Safonov, Y. G.; Bryzgalov, I. A.; Makovicky, E.; Balic-Zunic, T. Kudriavite, (Cd, Pb)Bi₂S₄, a New Mineral Species from Kudriavy Volcano, Iturup Island, Kurile arc, Russia. *Can. Mineral.* **2005**, 43, 695–701.
- (29) Ciobanu, C. L.; Brugger, J.; Cook, N. J.; Mills, S. J.; Elliott, P.; Damian, G.; Damian, F. MnBi₂S₄, a New Mineral from the Bǎja Bihor Skarn, Romania. *Am. Mineral.* **2014**, *99*, 1163–1170.
- (30) Topa, D.; Paar, W. H. Cupromakovickyite, Cu8Pb4Ag2-Bi18S36, a New Mineral species of the Pavonite Homologous Series. *Can. Mineral.* **2008**, *46*, 503–514.
- (31) Hwang, J.-Y.; Ahn, J. Y.; Lee, K. H.; Kim, S. W. Structural Optimization for Thermoelectric Properties in Cu-Bi-S Pavonite Compounds. J. Alloys Compd. 2017, 704, 282–288.
- (32) Cie & Stoe. X-Area, X-Red, and X-Shape, Darmstadt, Germany,

(33) Sheldrick, G. M. SHELXT- Integrated space-group and crystal-structure determination. *Acta Crystallogr., Sect. A: Found. Adv.* **2015**, 71, 3–8.

- (34) Mccarthy, T. J.; Ngeyi, S. P.; Liao, J. H.; Degroot, D. C.; Hogan, T.; Kannewurf, C. R.; Kanatzidis, M. G. Molten salt synthesis and properties of three new solid-state ternary bismuth chalcogenides, .beta.-CsBiS2, .gamma.-CsBiS2, and K2Bi8Se13. *Chem. Mater.* **1993**, 5, 331–340.
- (35) de Boor, J.; Gupta, S.; Kolb, H.; Dasgupta, T.; Muller, E. Thermoelectric Transport and Microstructure of Optimized Mg₂Si_{0.8}Sn_{0.2}. *J. Mater. Chem. C* **2015**, *3*, 10467–10475.
- (36) Perdew, J. P.; Burke, K.; Ernzerhof, M. Generalized Gradient Approximation Made Simple. *Phys. Rev. Lett.* **1996**, 77, 3865–3868.
- (37) Kresse, G.; Furthmüller, J. Efficient iterative schemes forab initiototal-energy calculations using a plane-wave basis set. *Phys. Rev. B: Condens. Matter Mater. Phys.* **1996**, *54*, 11169–11186.
- (38) Zunger, A.; Wei, S.-H.; Ferreira, L. G.; Bernard, J. E. Special Quasirandom Structures. *Phys. Rev. Lett.* **1990**, *65*, 353–356.
- (39) Asen-Palmer, M.; Bartkowski, K.; Gmelin, E.; Cardona, M.; Zhernov, A. P.; Inyushkin, A. V.; Taldenkov, A.; Ozhogin, V. I.; Itoh, K. M.; Haller, E. E. Thermal Conductivity of Germanium Crystals with Different Isotopic Compositions. *Phys. Rev. B: Condens. Matter Mater. Phys.* 1997, 56, 9431.
- (40) Morelli, D. T.; Heremans, J. P.; Slack, G. A. Estimation of the Isotope Effect on the Lattice Thermal Conductivity of Group IV and Group III-V Semiconductors. *Phys. Rev. B: Condens. Matter Mater. Phys.* **2002**, *66*, 195304.
- (41) Hao, S.; Shi, F.; Dravid, V. P.; Kanatzidis, M. G.; Wolverton, C. Computational Prediction of High Thermoelectric Performance in Hole Doped Layered GeSe. *Chem. Mater.* **2016**, 28, 3218–3226.
- (42) Makovicky, E.; Sotofte, I.; Karup-Moller, S. The Crystal Structure of Cu_{1.78}Bi_{4.73}Se₈, an *N*=3 Pavonite Homologue with a Cufor-Bi Substitution. *Z. Kristallogr.* **2006**, *221*, 122–127.
- (43) Mrotzek, A.; Kanatzidis, M. G. Tropochemical Cell-twinning in the New Quaternary Bismuth Selenides $K_x Sn_{6-2x} Bi_{2+x} Se_9$ and $KSn_5 Bi_5 Se_{13}$. *Inorg. Chem.* **2003**, *42*, 7200–7206.
- (44) Nakhal, S.; Wiedemann, D.; Stanje, B.; Dolotko, O.; Wilkening, M.; Lerch, M. LiBi₃S₅-A Lithium Bismuth Sulfide with Strong Cation Disorder. *J. Solid State Chem.* **2016**, 238, 60–67.
- (45) Mumme, W. G.; Watts, J. A. HgBi₂S₄: Crystal Structure and Relationship with the Pavonite Homologous Series. *Acta Crystallogr., Sect. B: Struct. Crystallogr. Cryst. Chem.* **1980**, *36*, 1300–1304.
- (46) Balic-Zunic, T.; Makovicky, E. The Crystal Structure of Kudriavite, (Cd,Pb)Bi₂S₄. Can. Mineral. **2007**, 45, 437–443.
- (47) Ruck, M.; Poudeu Poudeu, P. F.; Söhnel, T. Kristallstruktur und Elektronische Bandstruktur der Isotypen Sulfidchloride CuBiSCl₂ und AgBiSCl₂. Z. Anorg. Allg. Chem. **2004**, 630, 63–67.
- (48) Poudeu Poudeu, P. F.; Ruck, M. $Ag_{3.5}Bi_{7.5}S_{13}$, a New Member (N=8) of the Homologous Series $[Bi_2S_3]_2$. $[AgBiS_2]_{(N-1)/2}$. Acta Crystallogr., Sect. C: Struct. Chem. **2005**, 61, i41–i43.
- (49) Heerwig, A.; Thybaut, Cyril Louis C. L. J.; Ruck, M. Extended Occupational and Positional Disorder in Pavonite Homologous Copper Bismuth Chalcogenide Halogenides. *Z. Anorg. Allg. Chem.* **2010**, *636*, 2433–2438.
- (50) Poudeu, P. F. P.; Ruck, M. The Intergrowth Structure of $Ag_{1.2}Bi_{17.6}S_{23}Cl_8$ and its Relation to the Tubular Structure of $Bi_{6+\delta}S_{6+3\delta}Cl_{6-3\delta}$ and the Pavonite Homologue $Ag_{3x}Bi_{5-3x}S_{8-6x}Cl_{6x-1}$. *J. Solid State Chem.* **2006**, *179*, 3636–3644.
- (51) Wang, M.-F.; Jang, S.-M.; Huang, J.-C.; Lee, C.-S. Synthesis and Characterization of Quaternary Chalcogenides $InSn_2Bi_3Se_8$ and $In_{0.2}Sn_6Bi_{1.8}Se_9$. *J. Solid State Chem.* **2009**, *182*, 1450–1456.
- (52) Tan, G.; Hao, S.; Zhao, J.; Wolverton, C.; Kanatzidis, M. G. High Thermoelectric Performance in Electron-doped AgBi₃S₅ with Ultralow Thermal Conductivity. J. Am. Chem. Soc. **2017**, 139, 6467–6473
- (53) Kurosaki, K.; Kosuga, A.; Muta, H.; Uno, M.; Yamanaka, S. Ag₉TlTe₅: a High-Performance Thermoelectric Bulk Material with Extremely Low Thermal Conductivity. *Appl. Phys. Lett.* **2005**, 87, 061919.

(54) Brown, S. R.; Kauzlarich, S. M.; Gascoin, F.; Snyder, G. J. Yb₁₄MnSb₁₁: New High Efficiency Thermoelectric Material for Power Generation. *Chem. Mater.* **2006**, *18*, 1873–1877.

- (55) Guo, Q.; Chan, M.; Kuropatwa, B. A.; Kleinke, H. Enhanced Thermoelectric Properties of Variants of Tl₉SbTe₆ and Tl₉BiTe₆. *Chem. Mater.* **2013**, 25, 4097–4104.
- (56) He, Y.; Day, T.; Zhang, T.; Liu, H.; Shi, X.; Chen, L.; Snyder, G. J. High Thermoelectric Performance in Non-Toxic Earth-Abundant Copper Sulfide. *Adv. Mater.* **2014**, *26*, 3974–3978.
- (57) Zhao, L.-D.; Lo, S.-H.; He, J.; Li, H.; Biswas, K.; Androulakis, J.; Wu, C.-I.; Hogan, T. P.; Chung, D.-Y.; Dravid, V. P.; Kanatzidis, M. G. High Performance Thermoelectrics from Earth-Abundant Materials: Enhanced Figure of Merit in PbS by Second Phase Nanostructures. *J. Am. Chem. Soc.* **2011**, *133*, 20476–20487.
- (58) Liu, H.; Shi, X.; Xu, F.; Zhang, L.; Zhang, W.; Chen, L.; Li, Q.; Uher, C.; Day, T.; Snyder, G. J. Copper Ion Liquid-like Thermoelectrics. *Nat. Mater.* **2012**, *11*, 422–425.
- (59) Zhao, L.-D.; Lo, S.-H.; Zhang, Y.; Sun, H.; Tan, G.; Uher, C.; Wolverton, C.; Dravid, V. P.; Kanatzidis, M. G. Ultralow Thermal Conductivity and High Thermoelectric Figure of Merit in SnSe Crystals. *Nature* **2014**, *508*, 373.
- (60) Zhao, L.-D.; Tan, G.; Hao, S.; He, J.; Pei, Y.; Chi, H.; Wang, H.; Gong, S.; Xu, H.; Dravid, V. P.; Uher, C.; Snyder, G. J.; Wolverton, C.; Kanatzidis, M. G. Ultrahigh Power Factor and Thermoelectric Performance in Hole-doped Single-crystal SnSe. *Science* **2016**, *351*, 141–144.
- (61) Chang, C.; Wu, M.; He, D.; Pei, Y.; Wu, C.-F.; Wu, X.; Yu, H.; Zhu, F.; Wang, K.; Chen, Y.; Huang, L.; Li, J.-F.; He, J.; Zhao, L.-D. 3D charge and 2D phonon transports leading to high out-of-planeZTin n-type SnSe crystals. *Science* **2018**, *360*, 778–783.
- (62) Lin, H.; Tan, G.; Shen, J.-N.; Hao, S.; Wu, L.-M.; Calta, N.; Malliakas, C.; Wang, S.; Uher, C.; Wolverton, C.; Kanatzidis, M. G. Concerted Rattling in CsAg₅Te₃ Leading to Ultralow Thermal Conductivity and High Thermoelectric Performance. *Angew. Chem., Int. Ed.* **2016**, 55, 11431–11436.
- (63) Mukhopadhyay, S.; Parker, D. S.; Sales, B. C.; Puretzky, A. A.; McGuire, M. A.; Lindsay, L. Two-channel Model for Ultralow Thermal Conductivity of Crystalline Tl₃VSe₄. *Science* **2018**, *360*, 1455–1458.
- (64) Roychowdhury, S.; Jana, M. K.; Pan, J.; Guin, S. N.; Sanyal, D.; Waghmare, U. V.; Biswas, K. Soft Phonon Modes Leading to Ultralow Thermal Conductivity and High Thermoelectric Performance in AgCuTe. *Angew. Chem.* **2018**, *130*, 4107–4111.
- (65) Shi, Y.; Assoud, A.; Ponou, S.; Lidin, S.; Kleinke, H. A New Material with a Composite Crystal Structure Causing Ultralow Thermal Conductivity and Outstanding Thermoelectric Properties: Tl₂Ag₁₂Te_{7+δ}. J. Am. Chem. Soc. **2018**, 140, 8578–8585.
- (66) Dughaish, Z. H. Lead Telluride as a Thermoelectric Material for Thermoelectric Power Generation. *Phys. B* **2002**, 322, 205–223.
- (67) Sootsman, J. R.; Chung, D. Y.; Kanatzidis, M. G. New and Old Concepts in Thermoelectric Materials. *Angew. Chem., Int. Ed.* **2009**, 48, 8616–8639.